Multibaseline PolInSAR Using RADARSAT-2 Quad-Pol Data: Improvements in Interferometric Phase Analysis

Samira Alipour, Kristy F. Tiampo, Sergey Samsonov, and Pablo J. González

***Abstract*—We apply, for the first time, an equal-scattering-mechanism multibaseline optimization technique on quad-pol satellite images of RADARSAT-2 in order to increase the interferometric coherence. The optimized polarimetric channel results in the selection of new pixel candidates for multibaseline differential interferometric synthetic aperture radar applications, which, otherwise, are not recognized in any single-pol channel. In addition, we analyze the individual performance of this algorithm for rural and urban land covers along with the corresponding optimized scattering mechanisms. The optimized coherence improvement with respect to a single HH channel is shown to be correlated with the interferometric spatial and temporal baselines. Finally, we investigate the performance of this technique on the interferometric phase. The optimized interferograms increase the quality of the phase patterns with respect to those phases recovered in a single copolar channel, e.g., the residual orbital ramps of the RADARSAT-2 images.**

***Index Terms*—Differential interferometric synthetic aperture radar (DInSAR), equal scattering mechanism (ESM) multibaseline (ESM-MB) coherence optimization, pixel candidate (PC).**

I. Introduction

DIFFERENTIAL interferometric SAR (DInSAR) is a technique for measuring ground surface deformation. However, standard DInSAR is subject to decorrelation effects. The decorrelation of the signal can obscure the deformation phase and degrade the precision of DInSAR results. In recent years, the acquisition of large quantities of SAR data has led to the development of multibaseline DInSAR techniques [1]–[3]. These methods perform DInSAR analysis on a subset of pixels, as in the case of the persistent scatterer (PS) technique [2]. Ideally, the PS pixels return a stable backscatter signal through time. As a result, the phase signature of PS pixels is less affected by spatial and temporal decorrelation, resulting in a more reliable estimate of ground deformation. However, in order to identify PS pixels, a group of pixel candidates (PCs) with a higher S/N ratio must be selected, normally based on an amplitude dispersion index [3] or coherence criterion [4]. Accordingly, PS pixels are the PCs for which the phase stability criterion holds, e.g., with respect to nearby candidates [2]. This higher density of PCs and associated PS pixels provides a better estimate of the deformation over the relevant time periods.

Full polarimetric SAR (Pol-SAR) data provide additional information that can be used to increase the number of reliable points in an interferogram [5]. The choice of the best polarimetric channel reduces decorrelation noise and increases the number of pixels with increased coherence, which is one potential measure of the phase noise of an interferogram. Coherence optimization of Pol-SAR data is a technique which can be used to resolve dominant scatterers in a vertically structured media [6]. The first coherence optimization technique was presented by Cloude and Papathanassiou [7] and later expanded by others [8], [9]. Subsequently, this technique was extended to optimize the coherence of multibaseline interferograms simultaneously [10].

In this letter, for the first time, a multibaseline coherence optimization approach proposed by Neumann *et al.* [10] is applied to fully polarimetric spaceborne satellite data. Here, we use 15 images of the RADARSAT-2 satellite. These images which are acquired in quad-pol mode are used to investigate the performance of multibaseline polarimetric SAR interferometry (PolInSAR) coherence optimization. The study region is the San Francisco Bay area, adjacent to both the San Andreas and the Hayward faults, the region with the highest seismic hazard in northern California. Previous studies employed DInSAR and advanced DInSAR techniques on single channel data in order to study deformation along this fault [11], [12]. However, our objective is to use fully polarimetric data and integrate polarimetric and interferometric techniques in order to improve the quality of the resulting interferograms. In addition, we will investigate how the application of this technique enhances the number of PCs for multibaseline InSAR processing. The effects of variations in the spatial and temporal baseline interferograms also will be investigated.

II. PolInSAR

Fully Pol-SAR sensors measure the 2×2 scattering matrix S corresponding to each pixel. Under the reciprocity theorem, the off-diagonal elements are equal, and $S_{\mathrm{HV}} = S_{VH}$. The

Manuscript received March 4, 2012; revised June 6, 2012, September 5, 2012, and December 1, 2012; accepted December 21, 2012. This work was supported in part by the Natural Sciences and Engineering Research Council (NSERC) and Aon Benfield/Institute for Catastrophic Loss Reduction (ICLR) Industrial Research Chair (IRC) in Earthquake Hazard Assessment, an NSERC Discovery Grant, and an Ontario Early Researcher Award.

S. Alipour, K. F. Tiampo, and P. J. González are with the Department of Earth Sciences, Western University, London, ON N6A5B7, Canada (e-mail: salipou@uwo.ca; ktiampo@uwo.ca; pgonzal4@uwo.ca).

S. Samsonov was with the Department of Earth Sciences, Western University, London, ON N6A5B7, Canada. He is now with the Canada Centre for Remote Sensing, Ottawa, ON K1A0Y7, Canada (e-mail: Sergey.Samsonov@nrcan-rncan.gc.ca).

Digital Object Identifier 10.1109/LGRS.2012.2237501

scattering matrix is expressed as a vector using the Pauli basis as [7]

$$k_i = \frac{1}{\sqrt{2}}\left[S_i^{\mathrm{HH}} + S_i^{\mathrm{VV}}, S_i^{\mathrm{HH}} - S_i^{\mathrm{VV}}, 2S_i^{\mathrm{VH}}\right]^T \quad (1)$$

where the S_i^{HH} and S_i^{VV} are copolar terms and S_i^{VH} is the cross-polar term. i is the number of each set of quad-pol images, and ^{T} is the transpose operator.

PolInSAR forms an interferogram by projecting each SAR image pixel k on a corresponding scattering mechanism ω, resulting in a new pixel value λ. Performing this operation on a pixel-by-pixel basis will result in a new SAR image. By changing the polarization basis for both SAR images following (2), the corresponding interferogram is given by (3)

$$\lambda_i = \omega_i^{*T} k_i \quad (2)$$

$$\varphi_{ij_{(\omega_i,\omega_j)}} = \arg\left(\lambda_i \lambda_j^{*T}\right) = \arg\left(\omega_i^{*T}\Omega_{ij}\omega_j\right)$$

$$\Omega_{ij} = \langle k_i k_j^{*T}\rangle, \quad T_{ii} = \left\langle k_i k_i^{*T}\right\rangle \quad (3)$$

where $*$ represents the conjugate operator and $\langle\rangle$ is the multilooking factor. T_{ii} is the coherency matrix for SAR image i, and Ω_{ij} is the coherency matrix between two images i and j. Accordingly, $\varphi_{ij}(\omega_i, \omega_j)$ is the interferometric phase in the new polarimetric basis. Interferometric coherence $\gamma_{ij}(\omega_i, \omega_j)$ is calculated for two sets of SAR images in any arbitrary polarimetric basis defined by ω_i and ω_j as

$$\gamma_{ij}(\omega_i, \omega_j) = \frac{\omega_i^{*T}\Omega_{ij}\omega_j}{\sqrt{\omega_i^{*T}T_{ii}\omega_i\omega_j^{*T}T_{jj}\omega_j}}. \quad (4)$$

Coherence optimization consists of selecting those scattering mechanisms which provide the maximum coherence value. In the case of the equal scattering mechanism (ESM) multibaseline (ESM-MB) as proposed by Neumann *et al.* [10], the scattering mechanisms of the images remain the same among all the baselines $(\omega_i = \omega_j)$. However, this condition is not met using a multiple scattering mechanism (MSM) multibaseline (MSM-MB) technique $(\omega_i \neq \omega_j)$, and for every acquisition, an individual optimal polarization is found which correlates best to all others.

In previous research on DInSAR applications, the ESM has been applied in lieu of the MSM technique [5], for the primary reason that the MSM technique chooses various scattering mechanisms for each SAR acquisition. This can introduce an additional interferometric phase of the DInSAR method. While, in reality, some physical effects (e.g., change in soil moisture content, incident angle, and atmospheric conditions) will modify the scattering mechanisms between acquisitions, leading to temporal decorrelation, the change of the scattering mechanism between acquisitions might compensate for the temporal decorrelation in areas of less noise. Therefore, in some cases, the choice of MSM may provide better resolution of the interferometric phase. However, this is not guaranteed, and the choice of MSM can lead to the amplification of interferometric phase noise. As a result, for this study, ESM-MB was applied in order to provide a better understanding of the role of decorrelation in space and time.

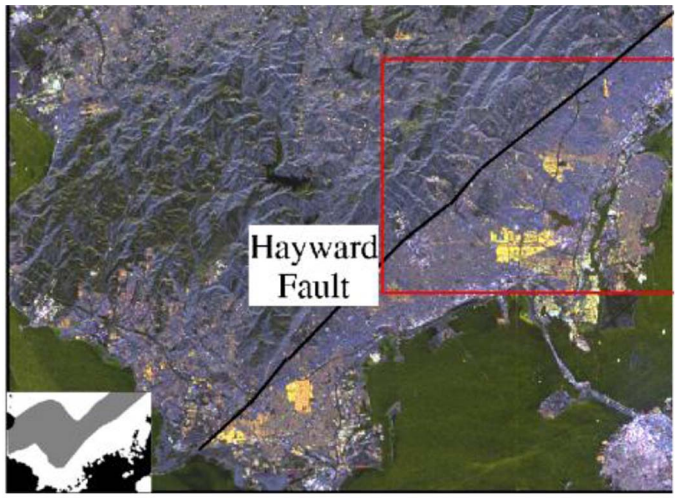

Fig. 1. RGB amplitude image of San Francisco city acquired from RADARSAT-2 satellite (R: HH channel, G: VV channel, B: VH channel). The black line delineates the approximate trace of the Hayward fault. The red square shows the close-up region used for interferometric analysis. The black-and-white figure shows the two subregions used for further analysis in Figs. 3 and 4. White and gray colors represent the urban and rural areas, respectively.

III. Application of Coherence Optimization Technique

We applied the ESM-MB coherence optimization algorithm proposed by Neumann *et al.* [10] for the first time to spaceborne SAR images acquired by the RADARSAT-2 satellite. The nominal height of the satellite is 798 km with a swath width of approximately 25 km. Polarimetric acquisition halves the swath width of the imaging SAR. The region is imaged from an incident angle of 18°–49° with a spatial resolution of ∼5 m. The performance of coherence optimization greatly depends on the configuration of the acquisition system, e.g., baseline lengths, acquisition times, and frequency [10]. Here, quad-pol optimization will be assessed on C-band imagery with a large number of baselines and a wider range of spatial and temporal separations. The study area is shown in Fig. 1. The black line approximately delineates the trace of the Hayward fault. The RGB image in this figure is representative of the amplitude images from three polarimetric channels (HH, VV, and VH), respectively. This area is covered by dense vegetation and rough topography in the middle of the image. The lower parts of this image are mainly composed of man-made structures.

As a proof of the concept, we chose 15 images, a subset of which was employed previously in a polarization phase difference analysis [13]. The SAR images were acquired at the following dates: 2008/04/26, 2008/06/13, 2008/07/07, 2008/07/31, 2008/12/22, 2009/01/15, 2010/09/07, 2010/10/01, 2010/10/25, 2010/11/18, 2010/12/12, 2011/01/05, 2011/01/29, 2011/02/22, and 2011/03/18. First, the Pol-SAR images were coregistered to subpixel accuracy. Later, all possible SAR pairs for interferogram formation were selected corresponding to three polarimetric channels (HH, VV, and VH). The number of possible interferograms corresponding to each polarimetric channel is 105. The spatial perpendicular baselines vary between 1 and 384 m, while the temporal baselines vary from 24 days to 3 years. Interferograms are formed with a multilooking

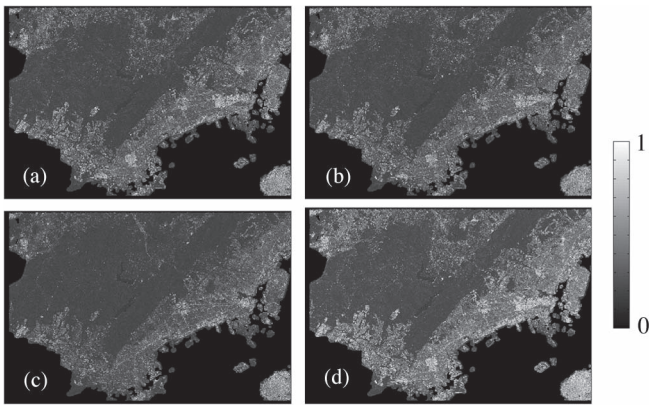

Fig. 2. Mean coherence maps. (a) HH, (b) VV, (c) VH, and (d) optimized images. Improvement of PolInSAR coherence (d) is clearly demonstrated with respect to single-pol channels (a)–(c).

factor of five in range and ten in azimuth (5×10), resulting in a final ground resolution of 24×47 m. Coherences are calculated by using a correlation window of 5×10 pixels.

Multibaseline coherence optimization was applied to the PolSAR images. The code is written in C++ language using the Lapack library[1] for efficient complex matrix operations. First, optimum scattering mechanisms (ω) were estimated and then applied using (2) to transform the pixels from the linear to the optimized polarimetric basis. Once this processing step was complete, the optimized SAR images were used to produce the coherences and interferograms between the same pairs, as detailed earlier for SAR images in (H,V) polarization basis, using (3) and (4). Then, the estimated optimized interferograms and coherences were compared with interferograms produced from single polarimetric channels.

IV. Performance of the Coherence Optimization Algorithm

Fig. 2(a)–(d) displays the mean coherence images retrieved from the interferometric stack of the HH, VV, VH, and optimized channels, respectively. Visual inspection of these figures confirms that coherence is enhanced significantly with respect to the single polarization estimates.

We divided the images into two subregions, rural and urban, identified in Fig. 1 by white and gray colors, respectively. Fig. 3(a)–(c) compares the mean coherences of the optimized and the HH channel associated with the entire image and the rural and urban subregions. Note that, in Fig. 3(c), the histogram of the urban region after optimization changes significantly, with most of the pixels tending to form a second peak at a much higher coherence than their initial HH coherences. This is the result of the abundance of man-made structures. The scarcity of these features for rural regions results in a modest coherence increment [see Fig. 3(b)].

Fig. 3(d)–(f) investigates the coherence improvement in terms of the number of PCs. The quality criterion used here for the selection of PCs is the mean coherence value computed over the interferogram stack. Here, the horizontal axis represents the coherence threshold, and the vertical axis represents the increment from the HH to the optimized channel in the percentage of PCs with respect to the total number of pixels in the entire image. Again, the percentage increase in PCs is calculated with respect to the entire image pixels, not with respect to those identified by the HH channel. For the urban area, the maximum increment in the percentage of PCs is $\sim$18%. For the rural area with higher topography and increased volume scattering from vegetation, the maximum increase in PCs reaches 10%. Note that many of these PCs are not detected in any single polarimetric channel, including HH, VV, or VH; for example, by using a coherence threshold of 0.3 for the entire image, this percentage increase is 7%. If we make the same comparison between the optimized channel with the average of three single polarimetric channels (HH, VH, and VV), we get a 10% increase in the number of newly selected PCs by applying the optimization procedure.

Fig. 3(g)–(i) displays the histogram of the α angle for the newly detected PCs in the optimized channel compared to the HH channel, using a coherence threshold of 0.3. The α angle represents types of the optimum scattering mechanisms derived from the parameterization of the optimized scattering vectors [14]. According to (5), the scattering vector is described by the scattering mechanism (α), orientation angle (β), ε, and μ as target phase angles. Here, we specifically consider the α which ranges between [0 90]°. Roughly speaking, α angles close to 0, 45°, and 90° correspond to surface scattering, volume scattering, and double bounce scattering, respectively

$$\omega = [\cos\alpha, \sin\alpha\cos\beta e^{i\varepsilon}, \sin\alpha\sin\beta e^{i\mu}]. \tag{5}$$

The results are shown for the (g) entire image pixels and the (h) rural and (i) urban subregions. Analysis of the results shows that histograms are mostly skewed toward higher α angles, representing pixels of double or even bounce scattering mechanisms. These scattering types are present in both the rural and urban subregions as, e.g., man-made structures. Moreover, the histogram of the rural subregion owns a secondary peak at lower α angles. This corresponds to scattering mechanisms from, e.g., rough surfaces where the optimization could differentiate some pixels as possible PC targets.

Fig. 4 shows the relationship between the relative coherence increment with respect to the HH channel for each individual spatial and temporal baseline corresponding to the (a) entire image, (b) rural subregion, and (c) urban subregion. In these figures, there is a clear relationship with the temporal and spatial separation of interferograms. Generally, for very short temporal and spatial baseline interferograms, we observe a smaller coherence increment. That the relative coherence improvement is stronger over larger baselines is related to lower initial coherence level.

Fig. 5 shows an interferogram between dates 2008/06/13 and 2011/03/18 for the enclosed region displayed in Fig. 1. This interferogram has a perpendicular baseline of 227 m and a temporal baseline of 1008 days. After the removal of topographic and flat earth phase components, the interferogram is dominated by a residual orbital component. To test the influence of the technique on the phase stability, we analyze the phase pattern, e.g., the residual orbital ramps.

[1]http://www.netlib.org/lapack/

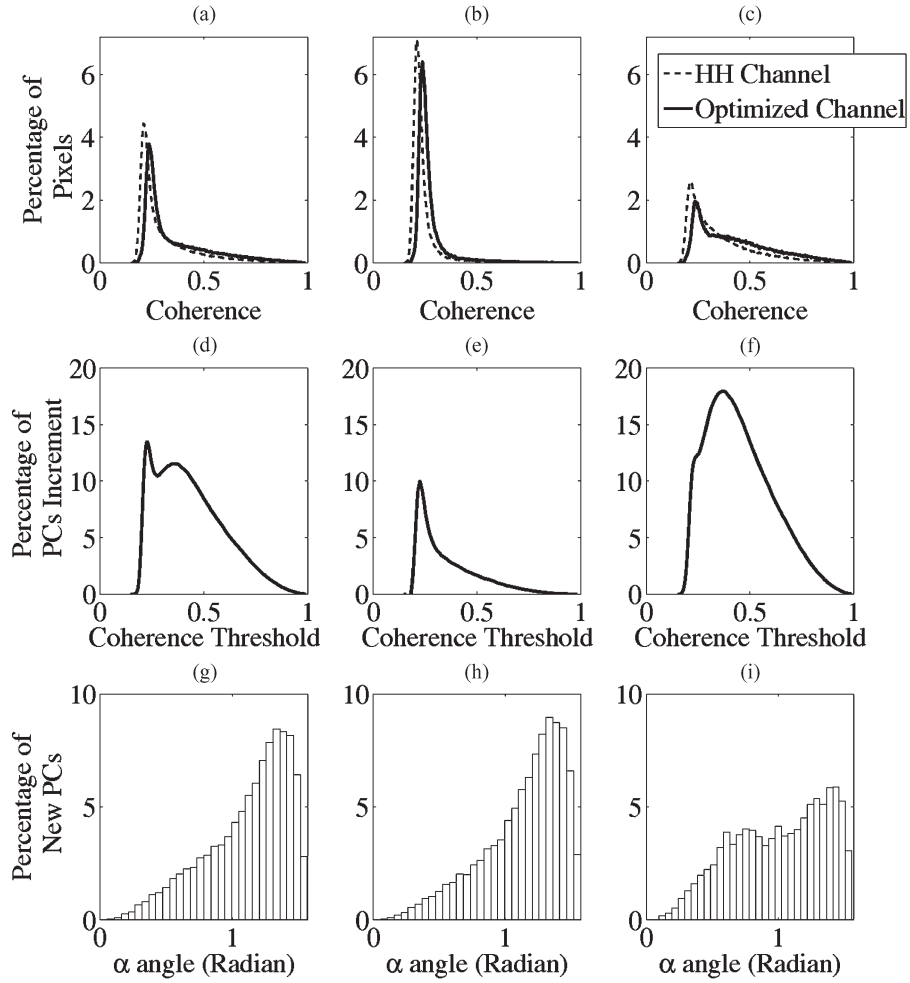

Fig. 3. (a)–(c) Histograms of the mean coherences for the HH and the optimized polarimetric channels associated with the (a) entire image and the (b) rural and (c) urban subregions. (d)–(f) PC increment after application of PolInSAR for an arbitrary coherence threshold. Here, the horizontal axis represents the coherence threshold, and the vertical axis is the increase in the number of PCs from the HH channel to the optimized channel, associated with (d) the entire image, (e) the rural subregion, and (f) the urban subregion. Note that the percentage is with respect to the entire image pixels. (g)–(i) Histogram of α angle for the newly selected PCs in the optimized channel compared to the HH channel (with coherence threshold of 0.3) for the (g) entire image pixels and the (h) rural and (i) urban subregions, respectively.

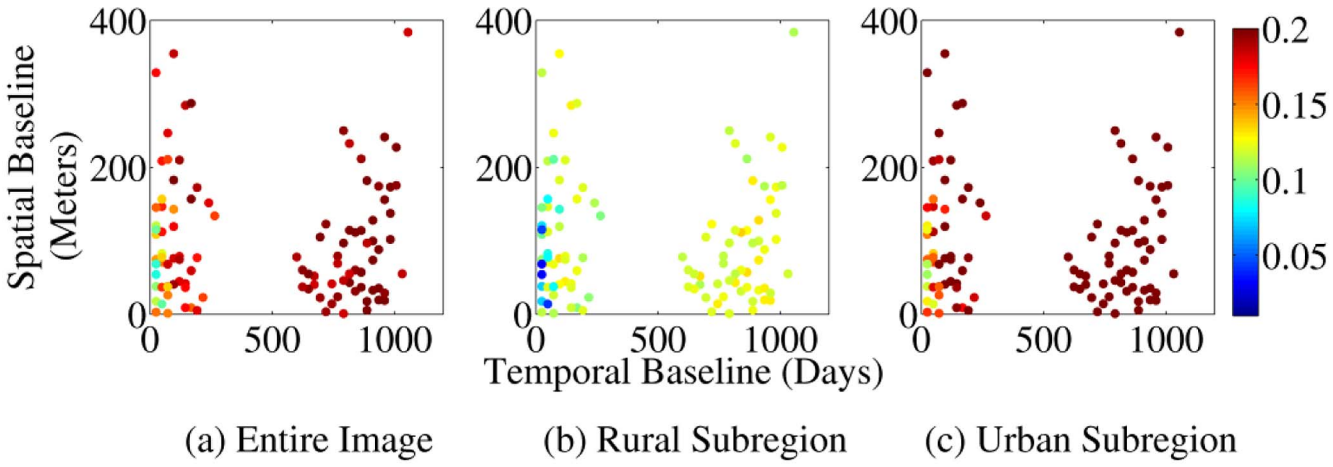

Fig. 4. (a)–(c) Relative mean coherence improvement (with respect to initial HH coherence) for individual interferograms of different spatial and temporal baselines, for the (a) entire image, (b) rural subregion, and (c) urban subregion.

Fig. 5(a) and (b) depicts the phase map for a segment of urban region with average coherence above 0.3, retrieved from the HH and optimized channels, respectively. These results show that the main interferogram features are well preserved after coherence optimization. In addition, the optimized phase patterns are slightly improved. To better show the phase quality

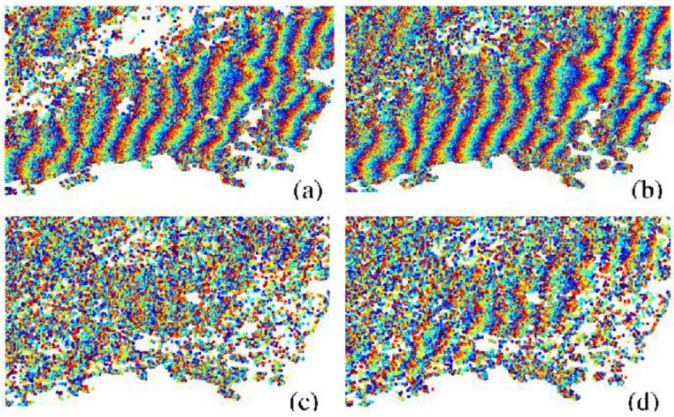

Fig. 5. Example of an interferogram formed between dates 2008/06/13 and 2011/03/18 for the close-up region in Fig. 1. (a) and (b) refer to the HH and optimized interferograms for pixels marked as PCs in each channel. (c) and (d) refer to the HH and optimized interferograms for pixels only marked as PCs in the optimized channel. Comparison of the interferograms shows that the main features of interferograms are preserved after application of PolInSAR technique. Comparing (c) and (d) shows that the quality of phase improves after application of PolInSAR technique.

improvement, we display the HH and optimized phases for pixels with average optimized coherence above 0.3 that were not selected with the previous HH coherence mask [see Fig. 5(c) and (d)]. Here, we clearly observe that the optimized interferograms increase the quality of the phase patterns with respect to HH phases. As a result, the apparent increase in the phase stability of the PolInSAR phase enhances the performance of multibaseline DInSAR, e.g., for better phase unwrapping.

V. Conclusion

Here, for the first time, we have applied the ESM-MB coherence optimization technique to satellite quad-pol images in order to increase the quality of the interferograms and retrieve a higher number of coherent PCs. The optimized interferograms provide a higher number of PCs which are not detected in any single-pol channels. In addition, we separately investigated the performance of the technique for urban and rural subregions. This improvement of coherence is shown to be dependent on the interferometric spatial and temporal baselines, and this varies with the subregion. Generally, for a very short temporal or spatial baseline interferogram, we observe a smaller coherence increment. Moreover, analysis of the optimized scattering mechanisms shows that most of the newly detected PCs in both rural and urban subregions correspond to the even bounce scattering types. These features are from man-made structures, which are more abundant in urban than rural subregions. Coherence optimization further improves scattering types in the rural subregion which are associated with rough surfaces.

The presented technique provides a promising method to recover more stable phase patterns (e.g., ground deformation) through the exploitation of fully polarized SAR images. In the future, we will compare the PolInSAR-ESM-MB and classical DInSAR techniques using single Pol-SAR data in order to fully illustrate the benefits of the proposed technique for ground deformation applications.

Acknowledgment

Images were acquired under Science and Operational Applications Research (SOAR-E) project 5024 from the Canadian Space Agency.

References

[1] P. Berardino, G. Fornaro, R. Lanari, and E. Sansosti, "A new algorithm for surface deformation monitoring based on small baseline differential SAR interferograms," *IEEE Trans. Geosci. Remote Sens.*, vol. 40, no. 11, pp. 2375–2383, Nov. 2002.

[2] A. Hooper, P. Segall, and H. Zebker, "Persistent scatterer InSAR for crustal deformation analysis, with application to Volcán Alcedo, Galápagos," *J. Geophys. Res.*, vol. 112, no. B7, pp. B07407-1–B07407-21, Jul. 2007.

[3] A. Ferretti, C. Prati, and F. Rocca, "Permanent scatterers in SAR interferometry," *IEEE Trans. Geosci. Remote Sens.*, vol. 39, no. 1, pp. 8–20, Jan. 2001.

[4] N. Adam, B. Kampes, and M. Eineder, "Development of a scientific permanent scatterer system: Modifications for mixed ERS/ENVISAT time series," in *Proc. Eur. Space Agency Spec.*, 2005, vol. ESASP-572, pp. 457–465.

[5] V. D. Navarro-Sanchez, J. M. Lopez-Sanchez, and F. Vicente-Guijalba, "A contribution of polarimetry to satellite differential SAR interferometry: Increasing the number of pixel candidates," *IEEE Geosci. Remote Sens. Lett.*, vol. 7, no. 2, pp. 276–280, Apr. 2010.

[6] K. P. Papathanassiou and S. R. Cloude, "Single-baseline polarimetric SAR interferometry," *IEEE Trans. Geosci. Remote Sens.*, vol. 39, no. 11, pp. 2352–2363, Nov. 2001.

[7] S. R. Cloude and K. P. Papathanassiou, "Polarimetric SAR interferometry," *IEEE Trans. Geosci. Remote Sens.*, vol. 36, no. 5, pp. 1551–1565, Sep. 1998.

[8] E. Colin, C. Titin-Schnaider, and W. Tabbara, "An interferometric coherence optimization method in radar polarimetry for high-resolution imagery," *IEEE Trans. Geosci. Remote Sens.*, vol. 44, no. 1, pp. 167–175, Jan. 2006.

[9] M. Qong, "Coherence optimization using the polarization state conformation in PolInSAR," *IEEE Geosci. Remote Sens. Lett.*, vol. 2, no. 3, pp. 301–305, Jul. 2005.

[10] M. Neumann, L. Ferro-Famil, and A. Reigber, "Multibaseline polarimetric SAR interferometry coherence optimization," *IEEE Geosci. Remote Sens. Lett*, vol. 5, no. 1, pp. 93–97, Jan. 2008.

[11] R. Bürgmann, E. Fielding, and J. Sukhatme, "Slip along the Hayward fault, California, estimated from space-based synthetic aperture radar interferometry," *Geology*, vol. 26, no. 6, pp. 559–562, Jun. 1998.

[12] R. Lanari, F. Casu, M. Manzo, and P. Lundgren, "Application of SBASD InSAR technique to fault creep: A case study of the Hayward Fault, California," *Remote Sens. Environ.*, vol. 109, no. 1, pp. 20–28, Jul. 2007.

[13] S. Samsonov and K. Tiampo, "Polarization phase difference analysis for selection of persistent scatterers in SAR interferometry," *IEEE Geosci. Remote Sens. Lett.*, vol. 8, no. 2, pp. 331–335, Mar. 2011.

[14] S. R. Cloude and E. Pottier, "An entropy based classification scheme for land applications of polarimetric SAR," *IEEE Trans. Geosci. Remote Sens.*, vol. 35, no. 1, pp. 68–78, Jan. 1997.